A Low-Latency, Low-Power CMOS Sun Sensor for Attitude Calculation using Photo-Voltaic Regime and On-chip Centroid Computation

Ruben Gomez-Merchan (iD), Juan Antonio Leñero-Bardallo (iD), *Member, IEEE*, María López-Carmona (iD),
and Ángel Rodríguez-Vázquez (iD), *Fellow, IEEE*

Abstract—The demand for sun sensors has skyrocketed in the last years due to the huge expected deployment of satellites associated with the New Space concept. Sun sensors compute the position of the sun relative to the observer and play a crucial role in navigation systems. However, the sensor itself and the associated electronics must be able to operate in harsh environments. Thus, reducing hardware and post-processing resources improves the robustness of the system. Furthermore, reducing power consumption increases the lifetime of microsatellites with a limited power budget. This work describes the design, implementation, and characterization of a proof-of-concept prototype of a low-power, high-speed sun sensor architecture. The proposed sensor uses photodiodes working in the photo-voltaic regime and event-driven vision concepts to overcome the limitations of conventional digital sun sensors in terms of latency, data throughput, and power consumption. The temporal resolution of the prototype is in the microsecond range with an average power consumption lower than 100 μW. Experimental results are discussed and compared with the state-of-the-art.

Index Terms—sun sensor, attitude control, low power, high speed, solar cell, continuous operation

I. INTRODUCTION

Obtaining the *sun vector* is a crucial information piece to determine the *attitude* of satellites and other spacecrafts and, hence, to help them navigate in outer space [1]–[3]. Because visible sunlight is ubiquitous in the regions where satellites navigate, visible-light electro-optical *sun sensors* are customarily employed for sun vector calculations [4]–[9]. In a CubeSat structure [2], for example, several sun sensors are required to achieve full sky coverage. Hence, with the expected large-scale deployment of satellites and micro-satellites [10], the sun sensors market volume will get the drive to grow significantly within the next few years.

A significant number of embarked sun sensors [11] consists of a few (typically four) photo-diodes that measure luminous sun intensity along several axes (typically North-East-South and West) [8], [9] - called *analog* sun sensors from now on. These analog sensors are fast because they have low pixel counts and provide analog signals with no Analog-to-Digital Conversion (ADC) required. However, they are sensitive to the light reflected by satellite superstructures and Earth albedo interference, resulting in sunspot artifacts [12] and incorrect sun vector calculations. Also, they require external (off the sensing chip) ADCs to interface with satellite control processors and are prone to communication errors [4], [5].

Alternative to analog ones, digital sun sensors employ CMOS active pixel arrangements with embedded ADCs [4]–[7]. Depending on the sun position, a Region of Interest (ROI) composed of a reduced group of pixels is illuminated, and the relative sun position (latitude and azimuth) is determined from the *centroid* of this ROI. Digital sun sensors overcome the analog communication issues of analog sensors at the assumable cost of increased sensing chip complexity with involved intra-chip pixel control waveforms [4], [5]. However, digital sensors are *data-centric* architectures that require encoding and communicating all pixel data (complete frames) despite the sparse optical scenes. Such a *data-centric* approach involves handling many information-less data and thus requires much more energy than is strictly needed and has inherent throughput limitations [13].

A way to overcome the drawbacks of conventional digital sun sensors while preserving their advantages versus analog counterparts is resorting to *information-centric* sensor concepts [13]–[15]. As opposed to conventional *data-centric* architectures, information-centric ones analyze the pixel data when they are acquired, extract the information contained in these data and encode and transmit information instead of raw pixel data. Sun sensors belonging to this class have been reported in [16] and [17]. They work such that the pixels illuminated by the sun disk autonomously calculate, using on-chip circuitry, the centroid coordinates, encoding them in the frequency of a digital pulse stream. Because information-less pixel data are neither read, encoded or transmitted, these sensors intrinsically achieve high speed with reduced energy consumption. Also, coding in the frequency domain benefits *high dynamic range* image capture [18]–[20], thus helping to reduce the impact of albedo.

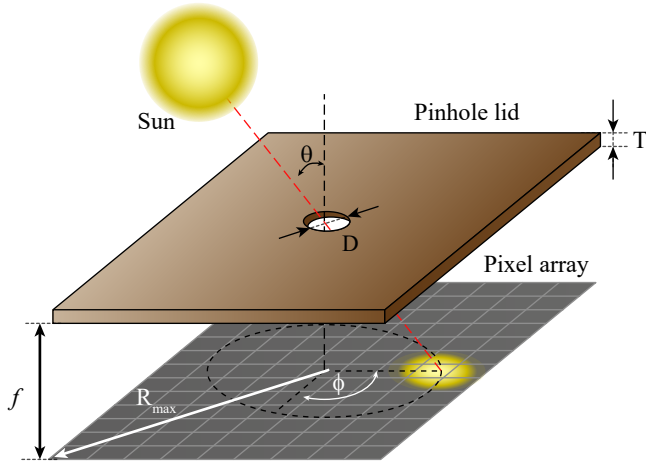This article reports a novel pixel with photo-diodes op-

Fig. 1. Sketch illustrating the sensor operation. The sun sensor is defined by the latitude, θ, and the azimuth, ϕ.

erating in a *photo-voltaic* regime, thus making a significant difference versus previous *information-centric* sun sensors that rely on the photo-conductive mode [16], [17]. When photodiodes are configured in the photo-voltaic mode, one terminal is floating and the junction voltage logarithmically depends on the incident optical power [21]. This voltage (usually called open-circuit voltage, Voc) is continuously generated in the pixel without using a trans-impedance amplifier. Thus, photodiodes operate as binary devices where a high voltage represents an illuminated pixel and a low voltage a dark one. In summary, the main advantages of the photo-voltaic mode include zero power consumption in the photoreceptor, continuous signal generation, and logarithmic compression. Besides using the photo-voltaic regime, the reported sensor incorporates low-power consumption asynchronous digital circuitry to directly compute the ROI centroid on-chip, remarkably simplifying the device operation and data exchange with other instruments and peripherals. Compared to existing commercial solutions, this new sensor meets the requirements [22] while featuring significantly lower power consumption and much higher operation speed in measurement per second - attributes that are very important to reduce the energy budget and hence the payload of embarked electronics [2]. The sensor architecture was advanced in a prior conference publication [23]. This paper provides more significant insights into the system implementation, the experimental characterization, and a discussion about the advantages over previous art.

II. SYSTEM'S PHYSICAL IMPLEMENTATION

Figure 1 is a sketch of the system implementation, consisting of an image sensor and a top pinhole lens. Because of this optical configuration, only a limited region (the ROI) is illuminated by the sun, the region itself changing with the sun position, the region itself changing with the sun position. The position of the sun is calculated from the centroid of the ROI, (x_c, y_c). Using these coordinates, the latitude, θ, and the azimuth, ϕ, are respectively calculated as follows [16]:

$$\theta = \arctan\left(\frac{\sqrt{W^2 \cdot (x_c - x_o)^2 + L^2 \cdot (y_c - y_o)^2}}{f}\right) \quad (1)$$

$$\phi = \arctan\left(\frac{L \cdot (y_c - y_o)}{W \cdot (x_c - x_o)}\right) \quad (2)$$

where W and L are the width and length of a single pixel, (x_o, y_o) is the centroid of the ROI, when $\theta = 0°$ and f is the focal distance between the pixel array and the lid. Note that versus implementations with more complex optic systems [17], pinhole lenses facilitate sensor calibration after fabrication, since the (x_o, y_o) point can be displaced from the centroid of the entire pixel array. This systematic error is easily corrected by processing the sensor data after calibration.

The maximum angle of incidence θ_{max} is limited by both the pixel array and the f of the lid. It can be calculated as a function of f, the dimensions of the pixels and the number of rows, M, and columns, N. This relationship is given by:

$$\theta_{max} = \arctan\left(\frac{R_{max}}{f}\right) \quad (3)$$

where R_{max} is the maximum radius of the sunlight projection on the pixel array, i.e., the maximum distance between the center of the array and one of the corners, which is determined by:

$$R_{max} = \frac{1}{2} \cdot \sqrt{(W \cdot M)^2 + (L \cdot N)^2} \quad (4)$$

The Field of View (FOV) is twice the maximum angle of incidence:

$$FOV = 2 \cdot \theta_{max} = 2 \cdot \arctan\left(\frac{R_{max}}{f}\right) \quad (5)$$

Since the FOV is inversely proportional to the f, this distance is crucial and must be minimized. In this prototype implementation, the pixel array dimensions are $M = N = 64$, the focal distance is limited by the package and equal to $f = 906$ μm, and pixel dimensions are $W = L = 19.5$ μm. Thus, the theoretical values of the FOV are 67.42º when the centroid moves horizontally throughout the sensor, and 88.67º for the maximum radius. This metric was not optimized and can be improved by reducing f.

III. IMAGE SENSOR ARCHITECTURE

The proposed sensor architecture targets reduced latency and power consumption to relax battery requirements in satellites. These targets involve two main strategies. On the one hand, the pixels generate a continuous voltage signal without consuming energy, so no exposure time is required to measure its voltage level. On the other hand, a combinational circuit uses the signals from the pixel array to compute the centroid of the illuminated region without the need for a clock to govern the operation of a sequential circuit. Figure 2 shows the block diagram of the proposed sensor. The prototype reported in the paper consists of an array of 64×64 pixels. The array includes
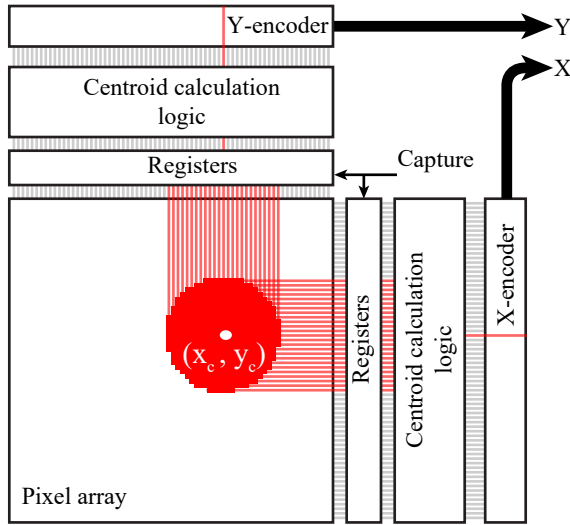
Fig. 2. Sensor block diagram. The main constitutive blocks are 1) The pixel array to detect the illuminated ROI. 2) 1-bit registers to latch the ROI-activated row/column lines. 3) The centroid calculation logic. 4) Encoders to send the centroid's coordinates off-chip.

$64 + 64$ *activation lines* (one per column in the array and one per row in the array); all pixels included in a given row (say row_i) share an activation line, and the same happens for all pixels in a given column (say col_j). When the pixel at (i,j) is illuminated by the sun, the associated activation lines (row_i and col_j) toggle, and the corresponding coordinates get stored in peripheral 1-bit register triggered by the external signal *capture*. The state of these registers defines the ROI. Based on this state, the centroid calculation logic extracts the central column and row of the ROI, namely the coordinates (x_c, y_c) of the centroid of the illuminated region.

Previously reported event-driven sun sensor chips [16], [17] employ a similar signaling and encoding strategy. However, these previous architectures require resetting the pixels and scanning the matrix to locate the illuminated area. A primary advantage of the architecture in this paper is that neither reset nor scanning is needed. Instead, the pixels' state is continuously updated independently of whether pixels are illuminated or not. This feature is a consequence of the operation of photodiodes in the photo-voltaic regime. It results in latency improvements by nearly one order of magnitude and a significant reduction of the power budget.

A. Pixel architecture

Figure 3 shows the pixel schematic consisting of the photodiode and the associated reset transistor, a comparator, and two output transistors used for signaling row and column activity, respectively. Transistors drawn in blue in the figure are shared per column and row outside the pixel array.

Note that the photodiode anode is floating during light capture. Thus, the photodiode operates in the photo-voltaic regime where the voltage drop from anode to cathode equals V_{oc}. Depending on the illumination conditions, this voltage
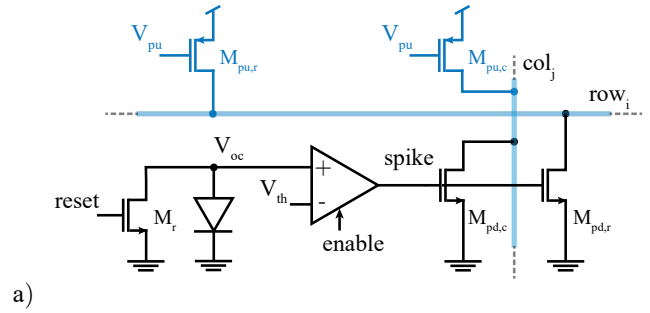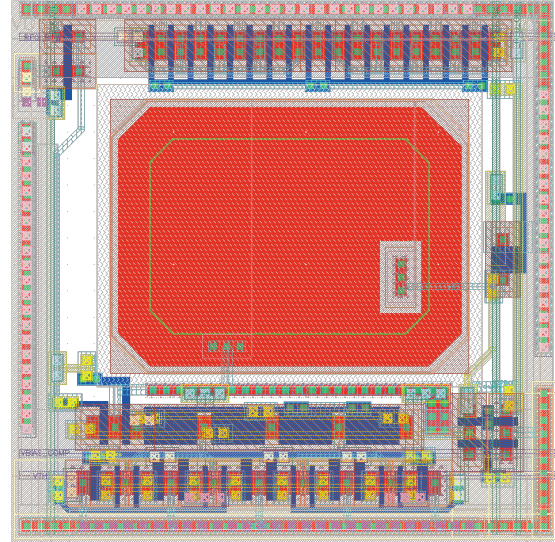
Fig. 3. a) Pixel schematics are composed of a photodiode working as a solar cell, a reset transistor, a comparator, and two pull-down transistors. Blue transistors make the pull-up networks. They are allocated outside the pixel array and shared by all the pixel matrix column and row lines. Transistors dimensions $\frac{W(\mu m)}{L(\mu m)}$ are: $M_r = 0.4/1$, $M_{pu,r} = M_{pu,c} = 8.1/0.2$ and $M_{pd,r} = M_{pd,c} = 9.9/0.2$. b) Pixel layout. The fill factor is 30.65% and the pitch is 19.5 μm.

typically ranges between 200 mV and 500 mV in CMOS technologies [24]. Note also that, excluding leakage and transient currents, there is no power consumption during capture, which is crucial to support the enhanced energy efficiency of the proposed architecture versus previously reported sun sensors.

The pixel comparator detects whether the photodiode's voltage is higher or lower than an adjustable threshold voltage, V_{th}. When V_{oc} is higher than V_{th}, the local digital signal *spike* gets activated, so that V_{th} sets the upper limit of the range where the pixel is considered as being illuminated. The row_i and col_j signals are the outputs of two distributed NOR gates implemented with pull-up transistor networks outside the matrix (blue transistors in Figure 3). They are active if there is at least one illuminated pixel in the *i-th* row and the *j-th* column.

Figure 4 shows the comparator schematic consisting of two stages. The first one is a 5T-OTA that operates in weak inversion to achieve low-power operation. The second one is a CMOS inverter used to isolate the front stage from the output
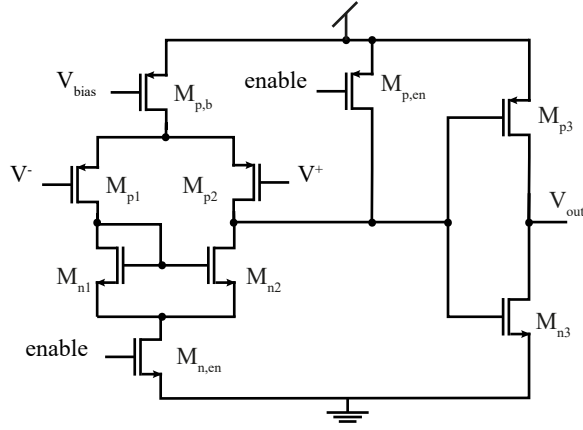
Fig. 4. Pixel comparator. Transistors dimensions $\frac{W(\mu m)}{L(\mu m)}$ are: $M_{p,b} = 7.04/0.4$, $M_{p1} = M_{p2} = 3.52/0.18$, $M_{n1} = M_{n2} = 0.88/2$, $M_{n,en} = M_{p,en} = 0.88/0.3$, $M_{p3} = M_{p4} = M_{n3} = M_{n4} = 0.44/0.3$.

node and hence increase the speed. There is also an enable transistor. When the enable signal is not activated, the output of the comparator is preset to a low level where there is no static current, thus vastly reducing the power consumption of the pixel array. The sensor can be made to enter into this idle state following a successful determination of the sun's position. The comparator power consumption is 4.88 nA operating and 43.33 pA in standby mode. The step-response delay introduced by the comparator under the former bias condition is 12.4 s.

The pixel can operate in two modes: the Integration Mode and the Continuous Mode.

1) Integration mode: This operation mode is intended to acquire the sun position on demand and set the sensor in standby mode afterward. Figure 5 (a) depicts the control signals timeline and the photodiode's transient voltage. After an initial reset, the photodiode integrates the charge. If it is illuminated, the voltage will tend to reach the open circuit voltage, V_{oc}, and thereafter a spike will be fired. When the control signal *capture* is activated, the centroid of the illuminated ROI will be calculated and transmitted off-chip.

Defining T_{int} as the time between the falling edge of $reset$ and the rising edge of $enable$, the latency of the sensor can be estimated as the addition of T_{int}; the comparator's delay, t_{comp}; the amount of time required to activate the row/column signals, t_{line}; the registers hold time, t_{hold}, and the propagation delay of the centroid calculation logic and the encoders, t_{logic}. Note that T_{int} must be active by a large enough time for the photodiodes to reach V_{th}. Thus, the pixel response time is

$$t_{pix} = T_{int} + t_{comp} + t_{line} \tag{6}$$

Note that the photodiode sensitivity, and hence T_{int}, depends on luminance. Also:

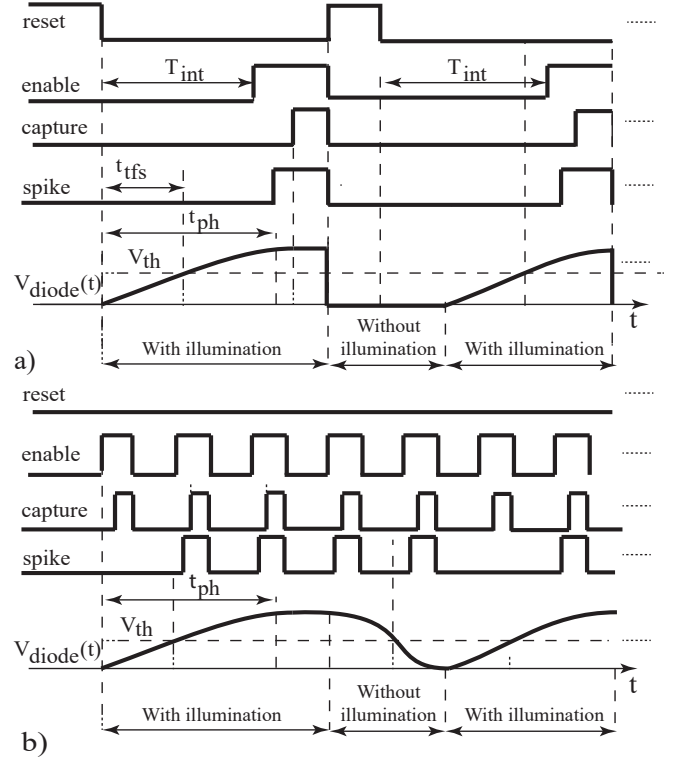$$T_{int} \gg t_{comp} + t_{line} + t_{hold} + t_{logic} \tag{7}$$

Fig. 5. Control signals timeline and photodiode transient voltage when the sensor operates in a) Integration Mode and b) Continuous Mode.

under average illumination conditions. Therefore, the latency, τ, is calculated as:

$$\tau = t_{pix} + t_{hold} + t_{logic} \simeq T_{int} \tag{8}$$

being limited by T_{int} and meaning that the temporal resolution of the sensor is determined by the sensitivity of the photodiode to variations in illumination.

2) Continuous mode: In this operation mode, the pixel operates continuously after an initial reset. As the chronogram in Figure 5 (b) shows, the photodiode voltage evolves to the open-circuit voltage, V_{oc} and does not remain locked at the reset value. If the comparator is enabled, the columns and rows of the illuminated pixels become active as soon as the pixels are illuminated. Then, the peripheral circuitry calculates the centroid of the ROI and transmits the pixel's coordinates off-chip. A positive edge of the external signal *capture* triggers the centroid calculation. If an external peripheral triggers the sun position calculation, it can enable the centroid computation either periodically with a sampling period, T_{sample} or selectively whenever the sun position has to be gauged. The pixel's time response to a local illumination variation, t_{pix}, depends on the photodiode's transient response t_{ph}, the comparator's latency, t_{comp}, and the amount of time required to pull the column/row signals down, t_{line}. Thus, $t_{pix} = t_{ph} + t_{comp} + t_{line}$.

It must be remarked that the pixel response time is much lower in the continuous mode, i.e. $t_{pix} << T_{int}$. The sensor latency time to an illumination variation, τ, is given by $\tau = t_{pix} + t_{hold} + t_{logic}$. This operation mode is much faster than
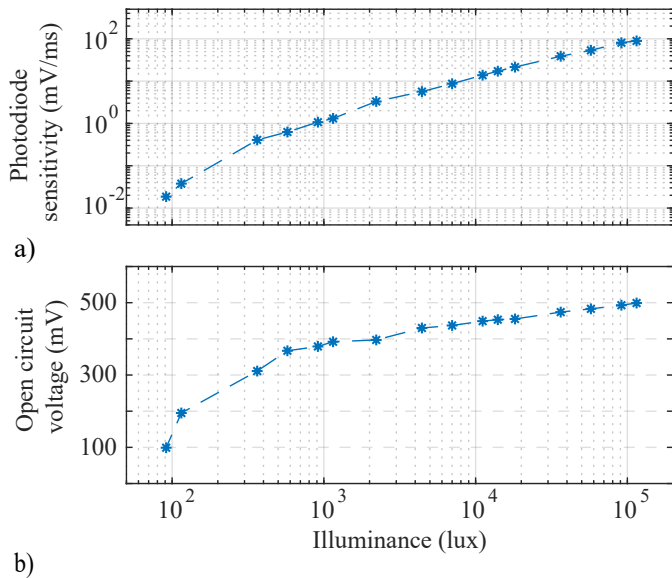
Fig. 6. Top: Photodiode sensitivity versus illumination. Bottom: measured open circuit voltage at T = 30 °C.
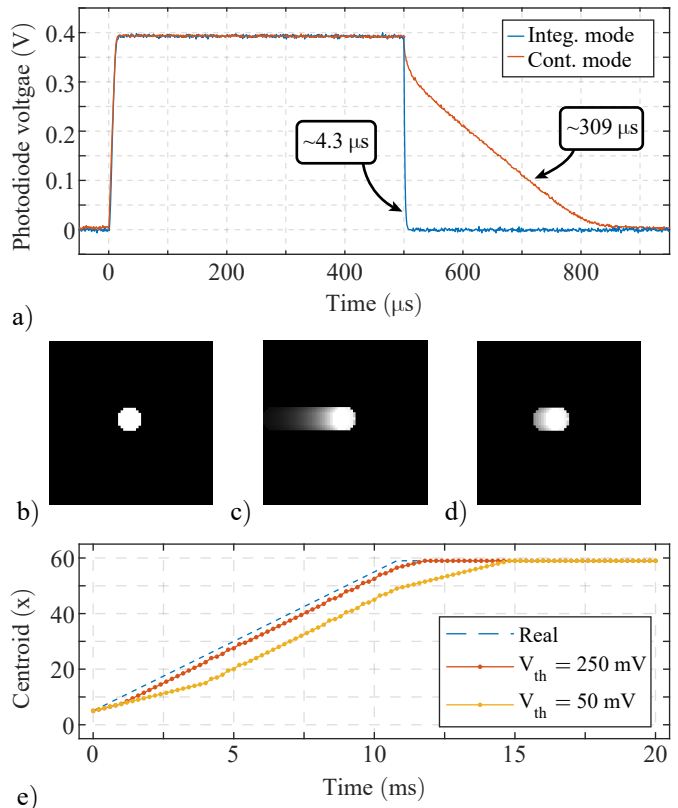

Fig. 7. a) Photodiode waveforms when illuminated with a pulsed laser at 1 kHz. b) Ideal image. c) Moving image showing the luminous trail. d) Luminous trail reduced with thresholding. e) Simulation results showing the transient error when calculating the x-coordinate of a fast-moving light source.

the previous one and is intended to track the sun's position with fine temporal resolution.

Figure 6 (a) depicts the measured photodiode sensitivity as a function of luminance. The sensitivity was inferred by measuring the slope of the photodiode voltage after resetting. T_{int} can be calculated using these data. In Figure 6 (b), the measured open circuit voltage is plotted against the chip luminance. This voltage ranges between 100 mV and 500 mV. We can estimate the photodiode latency by combining the data of both plots. For instance, if a pixel is suddenly exposed to 1 klux sunlight, with the comparator's threshold set to $V_{th} = 300$ mV, the amount of time required for the pixel to enable the activation line is 300 µs.

When a photodiode is no longer illuminated, the time it takes to discharge is proportional to the initial illumination value. In this situation, the photodiode voltage must transition from the V_{oc} voltage when it is illuminated to the dark voltage. Figure 7 (a) shows the voltage of a photodiode when illuminated with a pulsed laser at 1 kHz, showing a discharge time of $\sim$ 309 µs when it is not illuminated. The effect of the discharge time can be studied by modeling the behavior of the photodiodes as a first-order system with different time constants for rising and falling. Figure 7 (b) and (c) depict the ideal and real voltage of the photodiodes when the illuminated area moves horizontally at a speed of 5000 pixels/s, respectively, where white pixels represent the maximum V_{oc} (440 mV) value and black ones the minimum ($\sim$0 V). A luminous trail effect appears because of the slow discharge. This undesired effect is reduced by properly adjusting V_{th} as depicted in Figure 7 (d), where pixels with a voltage under 250 mV are considered dark pixels. Simulation transient results of the estimated centroid for different V_{th} values are represented in Figure 7 (e). We emulate a fast movement of

the centroid x-coordinate. The x-centroid coordinate estimation is plotted for different voltage threshold values. When the x-coordinate value reaches a steady value, the larger error in the x-coordinate computation observed by simulation is only two pixels for V_{th} = 250 mV.

B. Centroid calculation logic

Assume that a set of adjoining rows and columns are activated simultaneously at a given time. Then, the peripheral circuitry calculates the middle line utilizing a centroid calculation logic and sends it to a 6-bit encoder. Figure 2 illustrates this by showing in red the activated ROI rows/columns at the input of the centroid calculation logic. This module consists of several cascaded stages, as shown in Figure 8. Each stage behaves as an edge filter that detects and filters the pair of rows adjacent to a deactivated one (referred to as edges), thus meaning that more than one stage must be series-connected to complete the task. Because the size of the illuminated area is unknown and changes during operation, and the worst case corresponds to having M rows activated, including *M/2* stages guarantees a correct centroid computation independently of the ROI dimension.

Figure 10 represents the circuit corresponding to a single stage. The edge filter computes the AND operation with the two neighboring rows to detect whether an activated row is an
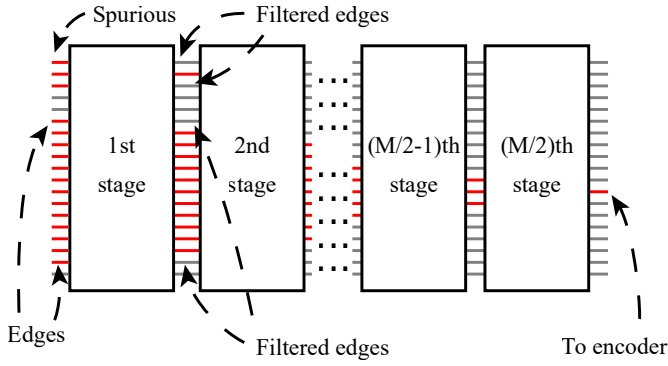
Fig. 8. Cascade connection of filtering stages in the centroid calculation logic. Red signals are activated while gray signals are deactivated.
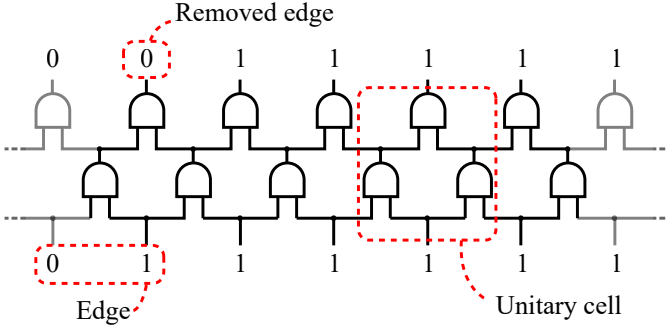

Fig. 9. Edge filter circuit computing the AND operation among neighboring signals. Signals on the bottom represent the input and signal on the top the output of the stage.

edge. Therefore, the *i-th* output element, out of the filtering stage, can be represented as:

$$out_i = in_{i-1} * in_i * in_{i+1}. \tag{9}$$

where in is the input vector. Therefore, out_i is activated only when in_i and the neighboring rows are also activated.

Nevertheless, when the input of Figure 9 has less than three activated bit lines, eq. (9) does not return any activated output line. This drawback is overcome by adding a multiplexer by stage, as depicted in Figure 10. Thus, if the signal $stage\_en$ is activated, the multiplexer transmits the output of the edge filter. This signal is the output of a distributed NOR, and it is activated only when at least one of the outputs of the edge filter is logic high, indicating there is valid data in that stage. Otherwise, if $stage\_en$ is deactivated, the multiplexer outputs the data from the last stage. Therefore, eq. (9) is reformulated as:

$$out_i = \begin{cases} in_{i-1} * in_i * in_{i+1}, & \text{if } \sum_{k=1}^{M} in_k \neq 0 \\ in_i, & \text{otherwise} \end{cases} \tag{10}$$

The registers must be reset once the centroid data is readout to reduce the time that a static current flows through the pull-up networks of the distributed NOR signals.

Note that this architecture is inherently robust against defective pixels since the activation of a row does not rely
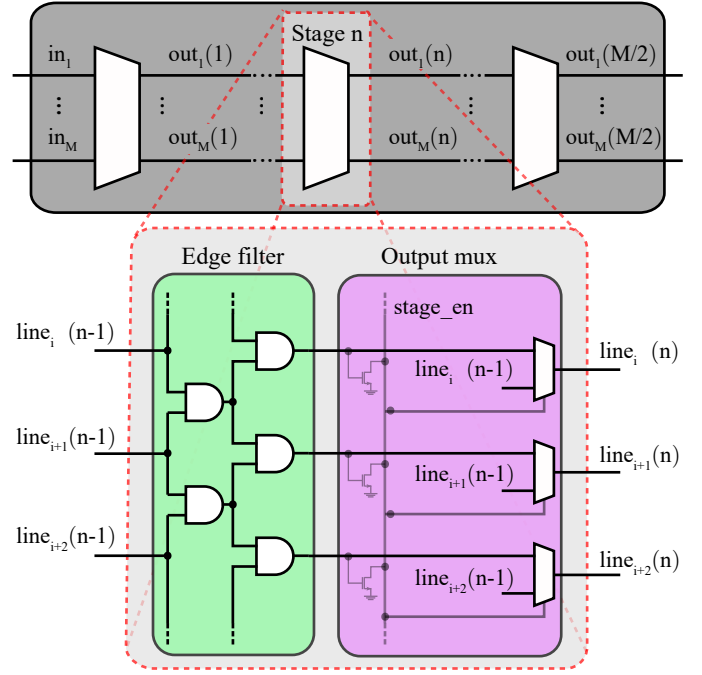

Fig. 10. Logic for centroid calculation, composed of $M/2$ cascaded stages. Each stage is composed of an edge filter and an output multiplexer.

on a single pixel but on all the illuminated pixels on that row. Furthermore, Figure 8 shows how spurious activated lines are filtered out when their dimension is lower than that of the ROI. This fact also increases the robustness of the proposed architecture if hot pixels activate the row under dark conditions, Earth albedo interference [12], or single radiation events effects [25].

Another situation that should be taken into account is when the output of the last stage has simultaneously two active bit lines. Since a pair of active bit lines will always be filtered in the next stage, the last stage includes a priority cell that detects when there are two activated lines. Figure 11 shows the implemented circuit. When the *i-th* and *(i+1)-th* lines are activated, another distributed NOR drives the $half\_pix$ signal low. In this way, only the *i-th* line is activated at the output. The $half\_pix$ signal improves the centroid coordinate resolution to half a pixel. However, this signal was not sent off-chip in this implementation because of the limited number of pads.
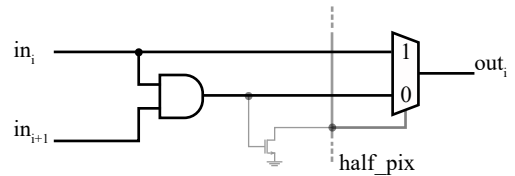

Fig. 11. Priority cell used in the last stage of the centroid calculation logic. There is one priority cell per row.

The proposed architecture presents several advantages compared to other circuits that compute the centroid on-chip. For instance, Massari et al. [26] presented an alternative

implementation to estimate the centroid of a light source. However, the power consumption is high, and it is hardly scalable since the pixel includes bipolar transistors. To the best of our knowledge, an asset of the proposed architecture over the existing ones is the continuous operation. That is possible because there is no reset phase. Consequently, the power consumption is much lower than in the previous architectures (see Table I).

C. Achieving sub-pixel resolution

Conventional sun sensors use the intensity level of each pixel to calculate the weighted average of the coordinates of the pixels and achieve sub-pixel resolution [4], [5]. Therefore, (x_c, y_c) can be expressed as:

$$x_c = \frac{\sum_{k=1}^{N_{pix}} DN_k \cdot x_k}{\sum_{k=1}^{N_{pix}} DN_k} \qquad (11)$$

$$y_c = \frac{\sum_{k=1}^{N_{pix}} DN_k \cdot y_k}{\sum_{k=1}^{N_{pix}} DN_k} \qquad (12)$$

where N_{pix} is the number of pixels used in the calculation of the centroid, and DN_k is the output digital number corresponding to the relative luminance value of each of those pixels. However, the architecture described in Section III uses the photodiodes as binary cells (1-bit encoding), limiting the resolution to half a pixel.

Oversampling the sensor output using different values of the comparator threshold (V_{th}) and computing the average increases the sensor resolution [26]. However, accuracy improvements are only guaranteed by relying on intensity data. Thus, using the intensity data becomes the only option. These intensity data are obtained by modifying the pixel and the architecture to work in the Time-to-First-Spike (TFS) mode [27], [28] with an Address Event Representation (AER) readout [29]–[31]. A companion sensor 64×64 sensor was integrated into the chip die to test and qualify this approach. When working in the TFS mode, photodiodes are reset, and the illumination level is time-encoded in the value of the interval needed for the photodiode to exceed the voltage threshold of a comparator (t_{tfs} in Figure 5). The AER readout height matches the height of the image sensor and has an area of 1248×70 μm^2. The pixel coincides with Figure 3 (a), but with one 1-bit-memory to store the state of the pixel, i.e., to block the pixel after readout. Note that the working principle of this pixel is the same as reported in Section III-A when the sensor operates in integration mode.

Both readout schemes co-exist at the hardware level and can be selected on demand, as Figure 12 illustrates. Thus, the complete architecture includes a coarse-acquisition mode (using the centroid calculation logic) and a fine-acquisition mode that achieves sub-pixel resolution. In this way, the coarse acquisition can be used to define the ROI, thus reducing the number of pixels that consume energy during TFS operation.
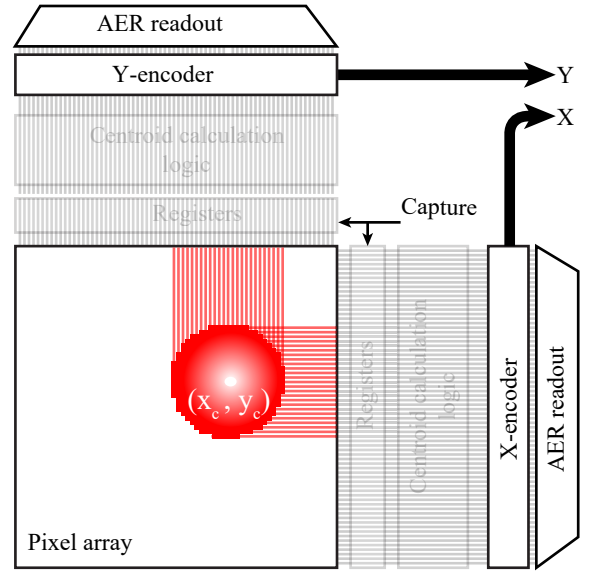

Fig. 12. Extended sensor architecture including an AER readout [29]–[31] architecture co-existing with the proposed architecture. This extra readout channel allows measuring the relative luminance of all pixels to achieve sub-pixel resolution.

IV. STATIC & DYNAMIC CHARACTERIZATION

Figure 13 (a) shows a microphotograph of the proposed sun sensor using the centroid calculation logic. Figure 13 (b) shows the top view of the system employed for experiments, including the pinhole lid glued to the sensor package. The sensor output was calibrated by rotating the position of an electronic angle finder with a light bulb attached to it. The sensor output data was recorded and displayed using a custom software interface shown in Figure 13 (c).

A. Calibration results

The static performance of the sensor when operating in continuous mode was measured through two different experiments. Using a light bulb attached to a digital angle finder, both the latitude and the azimuth were swept. Results are shown in Figure 14. To measure the latitude, the azimuth was kept constant and vice versa.

The minimum latitude and azimuth variation that can be measured correspond to one-pixel displacement. The peripheral circuitry for the centroid calculation provides the centroid expressed in pixel coordinates, e.g. (x_c, y_c) where x_c and y_c are integers. Thus, the latitude and azimuth resolution, $\Delta\theta$ and $\Delta\phi$, respectively, can be calculated as:

$$\Delta\theta = \arctan\left(pitch/f\right) \simeq pitch/f \qquad (13)$$
$$\Delta\phi = \arctan\left(1/R\right) \simeq 1/R \qquad (14)$$

where R is the radius (in pixel units) of the location of the centroid with respect to the center, yielding 1.23º and 3.81º (for R = 15 pixels), respectively.

In the TFS mode, the minimum latitude and azimuth variation corresponds to one digital code in the local luminance value of one pixel, since (x_c, y_c) is determined through a
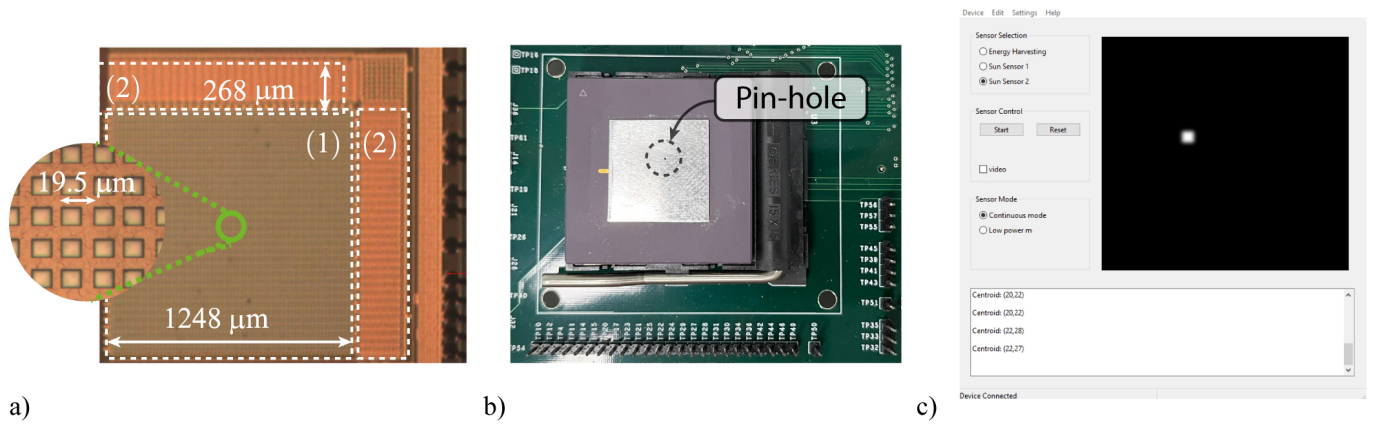
Fig. 13. a) Chip microphotograph of the continuous sensor: (1) Pixel array. (2) Peripheral circuitry. b) The top view of the test system shows the pin-hole lens glued to the sensor package; underneath, there is the chip socket and the PCB. c) Custom user interface for system debugging and control.

weighted average. Therefore, it can be deduced from eq. (11) and (12) that the resolution in the TFS mode is reduced by a factor of 2^n, where n is the effective number of bits in the measurement of the photocurrent. Thus, this figure improves to 0.0048° and 0.014°, respectively.

Furthermore, the theoretical value of the FOV calculated in Section II when the light source moves horizontally fits with the experimental results displayed in Figure 14 (a). The FOV could be increased by either increasing the number of pixels or reducing the focal distance of the optical setting.

B. Temporal response

As previously discussed in Section III-A, the sensor latency mainly depends on the amount of time required to detect the ROI with the illuminated pixels. In the integration mode, this time, T_{int}, is higher because the photodiode increases its voltage from approximately 0 V to the threshold voltage set at the comparator's input. Typically, $V_{th} = 250$ mV. In the continuous mode, the operation is faster because the diode voltage variations are gradual and continuous. During the integration mode, which defines the worst case, the sensitivity can be calculated as the slope of the curve from the experimental data of Figure 6 (a), resulting 1.24 mV/(µs· klux). Primary sensitivity limits are: i) the current flowing through the photodiode after a reset, and ii) the effective capacitance at the anode of the photodiode. If V_{th} is smaller enough than V_{oc}, this current can be assumed constant. Thus, the sensitivity can be increased by optimizing the capacitance, e.g., reducing the input capacitance of the comparator.

Thus, for $V_{th} = 250$ mV, the sensor latency can be expressed as 200 ms/lux. Usually, the frame rate is the standard parameter provided by manufacturers to indicate the latency of the digital sun sensor. To compare the speed of the proposed sensor to the state of the art, the sensor latency is equivalent to frame rates ranging from 150 kHz - 500 KHz for typical sunlight conditions without the use of attenuation filters. It must be pointed out that digital sun sensors require extra time to transmit and process the frames to determine the centroid which sometimes is not reported. In the proposed

implementation, the centroid is directly calculated by the peripheral logic in a very reduced amount of time, 31.5 ns.

Figure 17 shows the output sensor data when a bulb emulating the sun is moved manually over the system. The output was read out every 100 µs. That is equivalent in a frame-based sensor to 10,000 fps (frames per second).

On the other hand, Figure 16 shows the normalized output of the TFS mode using a 0.1 mm pin-hole lid. A total number of 248 pixels were readout in 158 ms. However, Figure 15 shows that the error in the measurement is lower than 2% even if all pixels are not readout [16]. Therefore, the latency and power consumption can be reduced by defining the number of pixels to be readout.

C. Accuracy & precision

The accuracy of the sensor when working in the continuous mode has been determined by processing the calibration data shown in Figure 14, resulting in 2.37° for the latitude and 5.82° for the azimuth (3σ). Figure 14 (a) shows that the error increases as the illuminated area begins to lie outside the pixel array. To mitigate this effect, the measured data were fitted with a 7th-order polynomial, extending the FOV up to 120° and reducing the error due to non-linearities. However, this calibration technique should be employed with extended data sweeping the coordinates of the centroid over the entire XY plane which was not possible with the available experimental setup. The deviation between the fitted curve and the experimental data leads to the error for each latitude value, achieving an accuracy of 0.78°. In this way, the accuracy is limited by the resolution and further work must be done to reduce this value, e.g., reducing the pixel pitch and f. To further increase the accuracy, the TFS mode can be used [16], at the cost of increasing power consumption and latency. The accuracy of the TFS mode was also obtained using calibration data and was found to be 0.012° for the latitude and 0.043° for the azimuth. However, it is not necessary to have information from all illuminated pixels. Figure 15 shows the measurement error and time depending on the number of read pixels. In this case, the error is less than 0.5% using the first 200 pixels.
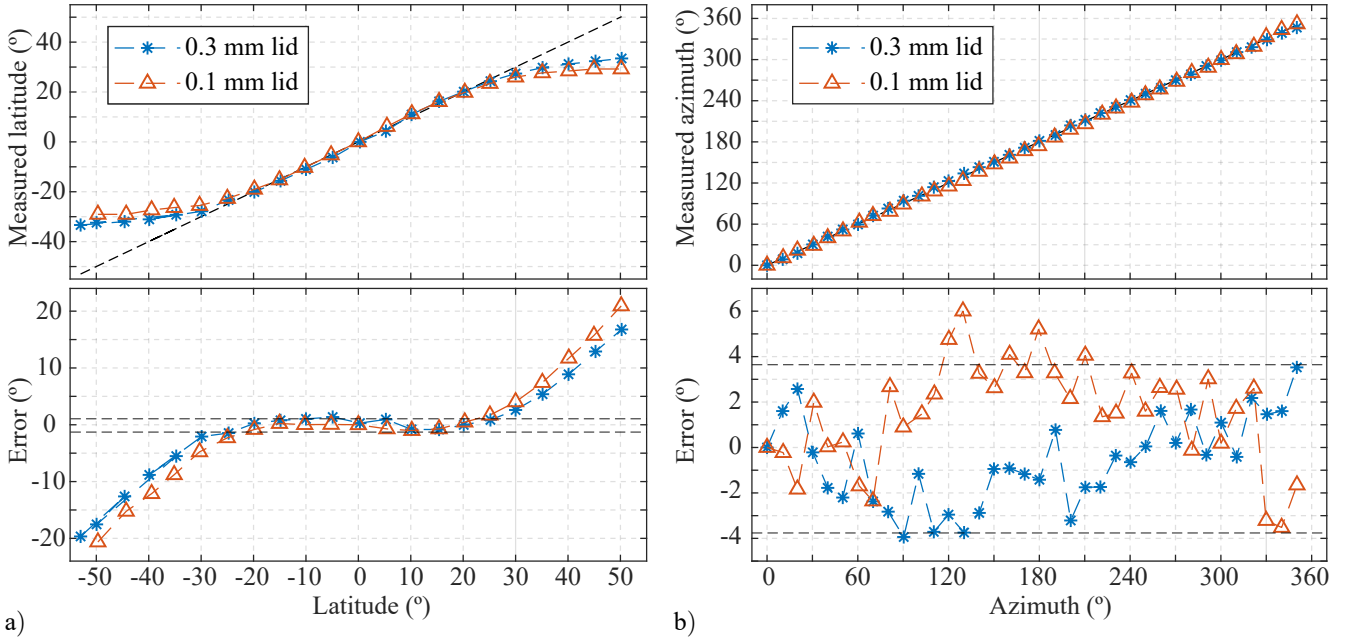
Fig. 14. Static characteristic absolute latitude and azimuth error of the sensor working in continuous mode with lids of 0.3 mm and a 0.1 mm hole diameter. The straight black lines represent the resolution of the sensor, i.e., 1.23º for the latitude and 3.81º for the azimuth.
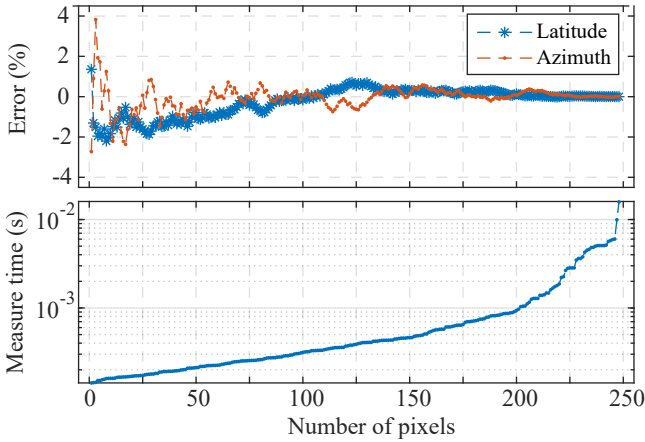

Fig. 15. Relative error and measure time as a function of the number of pixels used to calculate the centroid in the TFS mode.
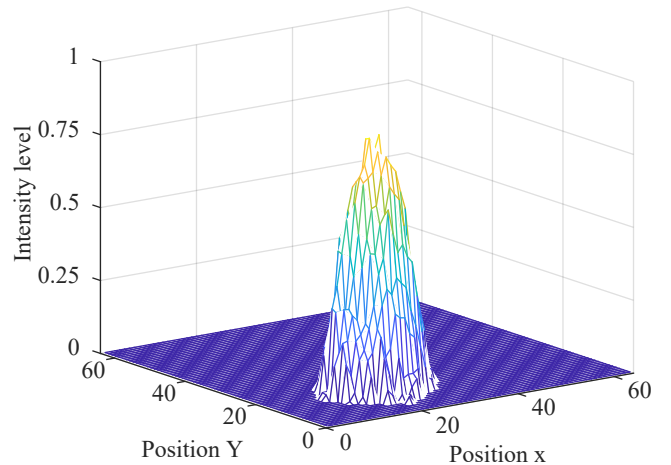

Fig. 16. Normalized sensor output, including the AER readout (TFS mode).

In sun sensors based on APS digital sensors [4], the principal source of random deviation is the pixel and ADC noise. On the contrary, for event-based sensors, the dominant source of noise comes from the collisions in the readout channel [16], which are reflected in temporal variations of the measured illumination level. Nevertheless, since the proposed architecture does not include any analog readout nor any shared bus for the readout, we have not observed the impact of random noise in the performed tests.

D. Power consumption

In the continuous mode, there are three primary sources of power consumption. The first one corresponds to the comparator in the pixel array, with a 20 μA static current (4.88 nA per pixel). The second one, with a current consumption of 85.4 μA/row, is associated with the distributed NOR gates that drive the pixels activation signals, as depicted in Figure 3. Although this current consumption might seem high, it only flows when the *spike* signal of the pixels is logic high. In the continuous mode, *spike* is activated straight after the pixel is enabled. Since the pixel can be disabled after the common signals are pulled down and registered, this time can be reduced to t_{line}, which is in the order of microseconds. In the integration mode, *spike* is disabled until the photodiode reaches V_{th}. In this way, the most illuminated rows and columns will consume energy before the least illuminated ones. However, the measured increment in energy consumption was not substantial when T_{int}
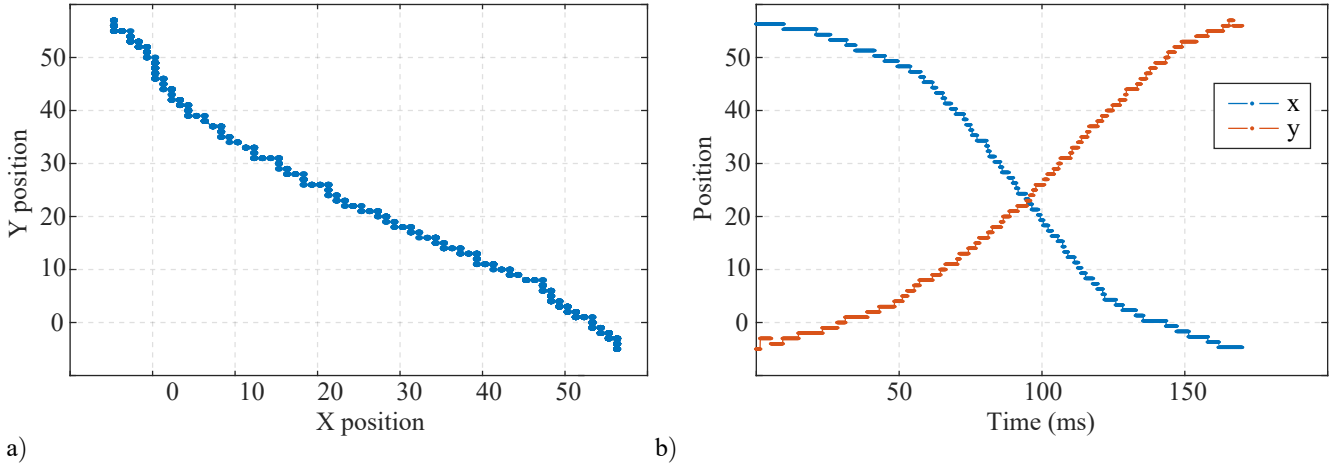
a)

b)

Fig. 17. Transient sensor response tracking a light bulb that was moved manually following a quasi-linear path. The sensor acquired 10,000 samples per second. a) Light source trajectory in the *XY*-plane, b) *X*- and *Y*-coordinates versus time.
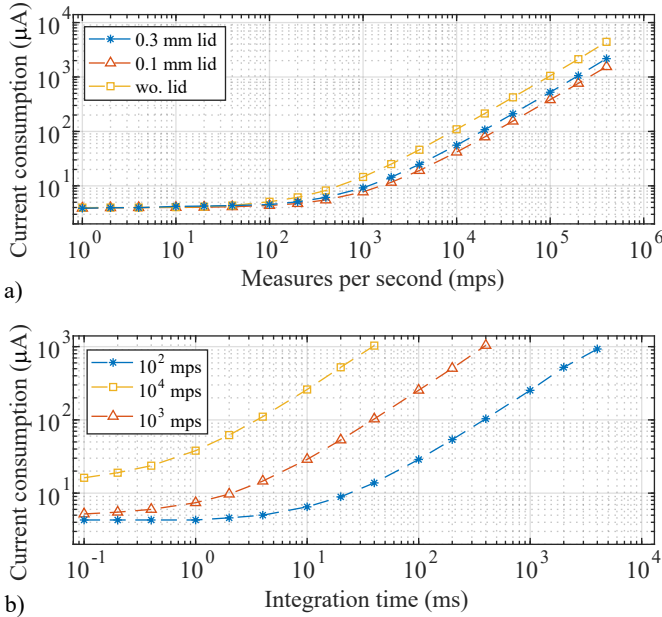

a)

b)

Fig. 18. Peripheral digital circuitry current consumption as a function of the a) frame rate and b) integration time.

was properly selected. The last one is the power consumption of the peripheral centroid calculation logic. The first source is static, while the last two depend on the operation speed.

In Figure 18 (a) the average current consumption of the peripheral circuit as a function of the measured rate is represented for different lid diameters and $T_{int} = 1$ µs. For low frame rates, the static current predominates (~ 4 µA), whereas for high rates the average current consumption increases linearly. Note that the larger the diameter (i.e., the illuminated area), the higher the power consumption, since more rows are pulled down because the ROI is larger. Figure 18 (b) shows the current consumption of the periphery as a function of the

integration time, for different measurement rates. It can be observed that the pull-up network is the dominant source of current consumption since the average current consumption depends linearly on the integration time.

The power consumption of the TFS mode can be divided into different sources: the power consumption of the pixel array, which does not vary from the continuous-mode implementation, and the power consumption of the AER readout block. The power consumption of the AER readout block depends only on the number of events transmitted to the external receiver. Since each illuminated pixel generates only one event, this power consumption is determined by the size of the illuminated area (i.e., the ROI) and scales linearly with the measurement rate. In this implementation, the current consumption of the AER readout block was 574 µA when the sensor acquired 1000 measurements per second. Each sample consists of output data of 248 pixels.

V. BENCHMARKING AND SCALABILITY

A. Benchmarking

Table I summarizes the performance of the proposed sensor and compares it with relevant state-of-the-art sun sensors. For comparison, four different devices have been considered. The first one is a prior event-based asynchronous sun sensor proposed by some of the authors [16]. The second one is a digital sun sensor with dedicated logic to detect the ROI [4]. Thus, once the ROI is detected, only the pixels inside it are readout. The penalty is a complex readout circuitry and the need to readout dark pixels to determine the ROI position. The third sensor corresponds to the Galileo ESA sun sensor [5]. It is a digital one with competitive specifications related to accuracy and resolution. The last one is a commercial analog sun sensor [9]. The main limitation of this sensor is the impossibility of identifying different light sources such as albedo.

The proposed architecture outperforms the state of the art in terms of temporal resolution, power consumption, and data

TABLE I
STATE-OF-THE-ART COMPARISON.

Work	This work (Continuous)	This work (TFS)	Leñero-Bardallo et al. [16]	Ning et al. [4]	Galileo ESA [5]	SSoC-DC60 [9].
Type	Continuous Mode Luminance Sensor	Event-based Luminance Sensor	Event Based Luminance Sensor	APS Digital Sensor	APS Digital Sensor	Analog sun sensor
Operation Principle	Solar cell	TFS	Octopus	Frame-based	Frame-based	Photo-current ratio
Technology	UMC 0.18 μm	UMC 0.18 μm	AMS 0.18μm HV	0.18 μm 1P4M	UMC 0.18 μm	ND
Power Supply	1.8 V	1.8 V	5/3.3 V	3.3/1.8 V	3.3/1.8 V	5 V
Chip Dimensions	1516 μm× 1516 μm	1318 μm× 1318 μm	4120 μm× 3315 μm	5 mm× 5 mm	11 mm× 11 mm	ND
Number of Pixels	64×64	64×64	128×96	368×368	512×512	2 pairs of photodiodes
Fill factor (%)	30.65	30.65	10	30	ND	NA
Pixel Pitch	19.5 μm	19.5 μm	25μm	6.5μm	11μm	NA
FOV (FOV/pix.)	88.67° (**0.98°**)	88.67° (**0.98°**)	146° (0.91°)	94° (0.18°)	128° (0.18°)	120°
Measurements per second (mps) / Frame rate (fps)	**5,000 mps@1klux** [a]	1000 fps@1klux	>200 fps@1klux	10 fps	10 fps	50 mps
Power Consumption	**63 μW @ 5,000 mps**	1.07 mW @ 1,000 mps	52 mW	42.73 mW	520 mW	350 mW
Dynamic Range	>100dB	>100dB	>100dB	52dB	ND	NA
Resolution	1.23°	0.0048°	0.03°	0.004°	<0.005°	ND
Accuracy	2.37°(θ), 5.82°(ϕ)	0.012°(θ), 0.043°(ϕ)	0.013°(θ), 0.05°(ϕ)	0.01°	0.024°	0.3°
Amount of data (acquisition / tracking mode)	**1 (centroid)**	1-100 Events	1-100 Events	368 pixels / 25×25 pixels = 945 pixels	1 frame / ROI	Centroid coordinates (with post-processing with a microcontroller)

ND: non disclosed by the authors. NA: non-applicable. Bold values are those where the sensor outperforms the art.

[a]The minimum time lapse between two consecutive measurements is either the inverse of the number of measurements per second or the inverse of the frame rate.

throughput. Over the digital ones, it is the only one that computes the ROI centroid on-chip and the only one whose dark pixels do not send output data. As further work, the sensor FOV, precision, and accuracy of the continuous mode can be improved by increasing the pixel array resolution and by reducing the pixel pitch. Examining Equations (5), (13) and (14), it is clear that the pixel pitch and the number of pixels limit these parameters. In the current implementation, the fill factor, 30.65%, is the highest for the benchmarked sensors.

B. Scalability and realibility

The sensor architecture is fully scalable. By increasing the number of pixels, the sensor latency and data throughput do not change. Only the static power associated with the analog blocks would scale proportionally to the number of pixels in the array. The low sensor latency can be exploited to detect radiation single events effects associated with space radiation by discarding fast and unexpected centroid variations. In case there is more than one ROI active in the sensor due to the albedo effect [12] or any spurious bit line activated by a SE, the proposed centroid logic calculation block automatically discards the smaller ROI to compute the centroid. The comparator voltage threshold can be adjusted to discriminate or detect ROIs with different illumination levels.

VI. CONCLUSIONS

This paper reports an innovative continuous-mode sun sensor architecture. One main novelty is linked to the use of photodiodes in the photo-voltaic regime, which prompts power consumption reductions above two orders of magnitude versus prior art. The sensor includes a dedicated logic to compute the centroid position to take advantage of the asynchronous nature of the photoreceptor stage and reduce data throughput and latency. Thus, the proposed architecture is less prone to communication errors since the only output data are the centroid coordinates. Furthermore, the proposed architecture is compatible with a TFS readout, which can be added in parallel in a future implementation to increase the sensor resolution.

REFERENCES

[1] Q. Fan, C. Chen, G. Wang, and X. Wei, "Parameters estimation of nutational satellite based on sun sensor," *IEEE Transactions on Instrumentation and Measurement*, vol. 71, pp. 1–8, 2022.

[2] P. Fortescue, G. Swinerd, and J. Stark, *Spacecraft Systems Engineering*, 4th ed. Wiley, 2011.

[3] E. Canuto, C. Novara, D. Carlucci, C. Perez-Montenegro, and L. Massott, *Spacecraft Dynamics and Control*, 1st ed. Butterworth-Heinemann, 2018.

[4] N. Xie and A. J. P. Theuwissen, "A miniaturized micro-digital sun sensor by means of low-power low-noise CMOS imager," *IEEE Sensors Journal*, vol. 14, no. 1, pp. 96–103, Jan 2014.

[5] F. Boldrini, E. Monnini, D. Procopio, B. Alison, W. Ogiers, M. Innocent, A. Pritchard, and S. Airey, "Attitude sensors on a chip: Feasibility study and breadboarding activities," in *Procceedings of 32nd Annual AAS Guided Control Conference*, February 2009, pp. 1197–1216.

[6] H. J. Kim, "A sun-tracking CMOS image sensor with black-sun readout scheme," *IEEE Transactions on Electron Devices*, vol. 68, no. 3, pp. 1115–1120, 2021.

[7] A. Ali and F. Tanveer, "Low-cost design and development of 2-axis digital sun sensor," *Journal of Space Technology*, vol. 1, no. 1, pp. 1–5, June 2011.

[8] P. Ortega, G. Lopez-Rodriguez, J. Ricart, M. Dominguez, L. M. Castaner, J. M. Quero, C. L. Tarrida, J. Garcia, M. Reina, A. Gras, and M. Angulo, "A miniaturized two axis sun sensor for attitude control of nano-satellites," *IEEE Sensors Journal*, vol. 10, no. 10, pp. 1623–1632, Oct 2010.

[9] "SSOC-D60 SOLARMEMS 2-axis digital sun sensor, https://www.cubesatshop.com/product/ssoc-d60-2-axis-digital-sun-sensor/. Last accessed: March 2021."

[10] S. Koechel and M. Langer, "New Space: Impacts of innovative concepts in satellite development on the space industry," in *69th International Astronautical Congress (IAC)*, 10 2018.

[11] L. Salgado-Conrado, "A review on sun position sensors used in solar applications," *Renewable and Sustainable Energy Reviews*, vol. 82, pp. 2128–2146, 2018. [Online]. Available: https://www.sciencedirect.com/science/article/pii/S1364032117311863

[12] D. Brasoveanu and J. Sedlak, "Analysis of Earth albedo effect on sun sensor measurements based on theoretical model and mission experience," in *AAS/GSFC 13th International Symposium on Space Flight Dynamics*, vol. 1, no. AAS-98-338, 1998.

[13] A. Rodríguez-Vázquez, J. Fernández-Berni, J. A. Leñero-Bardallo, I. Vornicu, and R. Carmona-Galán, "CMOS Vision Sensors: Embedding Computer Vision at Imaging Front-Ends," *IEEE Circuits and Systems Magazine*, vol. 18, no. 2, pp. 90–107, 2018.

[14] C. Posch, T. Serrano-Gotarredona, B. Linares-Barranco, and T. Delbruck, "Retinomorphic event-based vision sensors: Bioinspired cameras with spiking output," *Proceedings of the IEEE*, vol. 102, no. 10, pp. 1470–1484, Oct 2014.

[15] J. A. Leñero-Bardallo, R. Carmona-Galán, and A. Rodríguez-Vázquez, "Applications of event-based image sensors –Review and analysis," *International Journal of Circuit Theory and Applications*, vol. 46, 08 2018.

[16] J. A. Leñero-Bardallo, L. Farian, J. M. Guerrero-Rodríguez, R. Carmona-Galán, and A. Rodríguez-Vázquez, "Sun sensor based on a luminance spiking pixel array," *IEEE Sensors Journal*, vol. 17, no. 20, pp. 6578–6588, Oct 2017.

[17] L. Farian, P. Häfliger, and J. A. Leñero-Bardallo, "A miniaturized two-axis ultra low latency and low-power sun sensor for attitude determination of micro space probes," *IEEE Transactions on Circuits and Systems I: Regular Papers*, vol. 65, no. 5, pp. 1543–1554, May 2018.

[18] E. Culurciello, R. Etienne-Cummings, and K. Boahen, "A biomorphic digital image sensor," *Solid-State Circuits, IEEE Journal of*, vol. 38, no. 2, pp. 281–294, Feb 2003.

[19] J. A. Leñero-Bardallo, R. Carmona-Galán, and A. Rodríguez-Vázquez., "A bio-inspired vision sensor with dual operation and readout modes," *Sensors Journal, IEEE*, vol. 16, no. 2, pp. 1–14, January 2016.

[20] J. A. Leñero-Bardallo, D. Bryn, and P. Häfliger, "Bio-inspired asynchronous pixel event tricolor vision sensor," *Biomedical Circuits and Systems, IEEE Transactions on*, vol. 8, no. 3, pp. 345–357, June 2014.

[21] S. Donati, *Photodetectors: devices, circuits and applications*. John Wiley & Sons, 2021.

[22] C.C. Liebe, "Star trackers for attitude determination," *IEEE Aerospace and Electronic Systems Magazine*, vol. 10, no. 6, pp. 10–16, 1995.

[23] R. Gomez-Merchan, M. López-Carmona, J. A. Leñero-Bardallo, and A. Rodríguez-Vázquez, "A high-speed low-power sun sensor with solar cells and continuous operation," in *ESSCIRC ESSDERC 2021 European Solid-state Circuits and Devices Conference*. IEEE, 2021, pp. 1–4.

[24] R. Gómez-Merchán, D. Palomeque-Mangut, J.A. Leñero-Bardallo, M. Delgado-Restituto and A. Rodríguez-Vázquez, "A Comparative Study of Stacked-Diode Configurations Operating in the Photovoltaic Region," *IEEE Sensors Journal*, vol. 20, no. 16, pp. 9105–9113, 2020.

[25] ECSS, *Techniques for radiation effects mitigation in ASICs and FPGAs handbook*. ECSS Secretariat, ESA-ESTEC Noordwijk, The Netherlands, 2016.

[26] N. Massari *et al.*, "High speed digital CMOS 2D optical position sensitive detector," in *Proceedings of the 28th European Solid-State Circuits Conference*. IEEE, 2002, pp. 723–726.

[27] C. Shoushun and A. Bermak, "A low power CMOS imager based on time-to-first-spike encoding and fair AER," in *2005 IEEE International Symposium on Circuits and Systems*, 2005, pp. 5306–5309 Vol. 5.

[28] C. Shoushun and A. Bermak, "Arbitrated time-to-first spike CMOS image sensor with on-chip histogram equalization," *Very Large Scale Integration (VLSI) Systems, IEEE Transactions on*, vol. 15, no. 3, pp. 346–357, March 2007.

[29] M. Mahowald, *An Analog VLSI System for Stereoscopic Vision*. Kluwer, 1994.

[30] A. Mortara, E.A. Vittoz and P. Venier, "A communication scheme for analog VLSI perceptive systems," *IEEE Journal of Solid-State Circuits*, vol. 30, no. 6, pp. 660–669, 1995.

[31] K. A. Boahen, "Point-to-point connectivity between neuromorphic chips using address events," *IEEE Transactions on Circuits and Systems II*, vol. 47, no. 5, pp. 416–434, 2000.